

This work was written as part of one of the author's official duties as an Employee of the United States Government and is therefore a work of the United States Government. In accordance with 17 U.S.C. 105, no copyright protection is available for such works under U.S. Law.

Public Domain Mark 1.0

<https://creativecommons.org/publicdomain/mark/1.0/>

Access to this work was provided by the University of Maryland, Baltimore County (UMBC) ScholarWorks@UMBC digital repository on the Maryland Shared Open Access (MD-SOAR) platform.

Please provide feedback

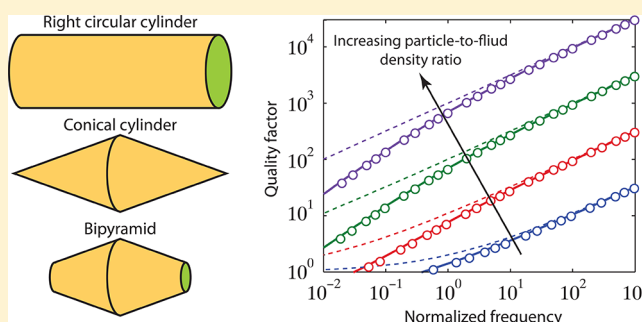
Please support the ScholarWorks@UMBC repository by emailing scholarworks-group@umbc.edu and telling us what having access to this work means to you and why it's important to you. Thank you.

Vibration of Nanoparticles in Viscous Fluids

Debadi Chakraborty,[†] Emma van Leeuwen,[†] Matthew Pelton,[‡] and John E. Sader^{*,†,§}[†]Department of Mathematics and Statistics, The University of Melbourne, Victoria 3010, Australia[‡]Center for Nanoscale Materials, Argonne National Laboratory, Argonne, Illinois 60439, United States[§]Kavli Nanoscience Institute and Department of Physics, California Institute of Technology, Pasadena, California 91125, United States

S Supporting Information

ABSTRACT: The dynamics of mechanical structures can be strongly affected by the fluid in which they are immersed. Ultrafast laser spectroscopy has recently provided fundamental insight into this fluid-structure interaction for nanoparticles immersed in a range of viscous fluids. In this article, we present results of a rigorous finite-element analysis and commensurate scaling theory that enable interpretation and analysis of these experiments, for the extensional vibrational modes of axisymmetric nanoparticles immersed in viscous fluids. Right circular, conical, and bipyramidal axisymmetric cylinder geometries are considered. We also develop an approximate analytical model that accounts for finite viscous penetration depth, which displays excellent agreement with finite-element results for particles of large aspect ratio. The finite-element results agree well with available measurements for particles in low-viscosity fluids such as water, but significant discrepancies exist at higher viscosities. Possible mechanisms for these differences are discussed.



1. INTRODUCTION

Acoustic vibrations of nanoparticles have been studied extensively over the past 15 years, using frequency-domain methods such as Brillouin scattering¹ and Raman scattering^{2–4} and time-domain approaches such as transient-absorption spectroscopy.^{5–21} This body of work has demonstrated that the standard theory of elasticity using bulk material properties applies to such nanoscale structures, with excellent agreement between measurement and theory.^{22–24} This property has been demonstrated over a wide range of particle sizes, down to particles consisting of only a few hundred atoms.²⁰

These studies have direct implications for a host of applications that utilize nanoscale materials, allowing for the use of continuum principles in modeling, design, and measurement interpretation.^{25,26} In particular, devices based on mechanical vibrations of nanoscale structures are currently being explored as versatile platforms for physical, chemical, and biological sensors.^{27–38}

High detection sensitivity in nanomechanical devices requires low damping—i.e., high-quality factors—to enable precise measurement of their dynamic response. Energy loss mechanisms thus limit this detection sensitivity.²⁵ This is of particular concern for the operation of sensors in a fluid environment, where viscous dissipation⁷ and acoustic radiation losses^{25,39} can be considerable. While the acoustic resonant frequencies of nanoparticles have been widely studied,^{5–21} the damping rates for nanoparticles in fluid have only recently been measured.^{7,8,12} Primary factors limiting such measurements are

that (i) nanoparticle synthesis techniques often produce samples with significant polydispersity in size and shape and (ii) measurements are most often performed on ensembles of such nanoparticles. Since the resonant frequency of a nanoparticle depends on its shape, size, and elastic properties, such polydispersity induces significant dephasing of the ensemble response. Such inhomogeneous dephasing can completely mask the true damping properties of individual nanoparticles, hindering measurements of mechanical energy dissipation.

An immediate remedy is to study the dynamics of a single nanoparticle deposited on a substrate.^{21,40–44} In this case, however, there is mechanical coupling between the particle and the substrate, which introduces an unknown and variable degree of damping. This substrate damping complicates measurement analysis, making it difficult to determine the degree of energy damping due to other mechanisms. Recently, we showed that inhomogeneous dephasing could be reduced by using highly monodisperse bipyramidal gold nanoparticles.^{7,8} These samples enabled damping of the acoustic vibrations in an ensemble of nanoparticles to be measured for the first time. Since these measurements were performed in liquid, away from any surface, damping due to the liquid could be determined directly and quantitatively. Very recent work has significantly

Received: January 31, 2013

Revised: March 21, 2013

Published: March 21, 2013



improved on these studies by performing measurements on single particles that were optically trapped in liquid.¹² Measurements were performed on single nanorods and nanospheres. While the results for spheres were compared to available theory, the results for rods were not analyzed theoretically. Here, we provide theoretical results that enable interpretation and analysis of such measurements and future studies of extensional acoustic vibrations in cylindrical nanoparticles.

These results build on an approximate analytical model that we proposed earlier.^{7,8} This approximate model uses elastic rod theory and implicitly assumes that the particle has a very large aspect ratio (particle length/radius). The hydrodynamic load exerted by the surrounding fluid is determined using a local analysis involving Stokes' second problem;⁴⁵ the theory thus implicitly assumes thin viscous penetration depths relative to the particle diameter. Although good agreement with measurements on bipyramidal particles was demonstrated,^{7,8} the accuracy of this approximate model is yet to be established for particles of finite aspect ratio and finite viscous penetration depth.

In this article, we present a detailed numerical investigation of the dynamic response of axisymmetric nanoparticles immersed in viscous fluids. This is achieved using finite-element simulations of the fluid-structure problem. Deformation of the solid is described by Navier's equation, the fluid is described by the Navier-Stokes equation, and coupling between these complementary continuum theories is implemented directly and rigorously. Since the typical particle size greatly exceeds the molecular length scale of the surrounding fluid, a continuum treatment is expected to be valid. The resulting numerical data are nondimensionalized using an exact scaling theory, making it possible to derive numerical results of a general nature. Complementary to this numerical study, we present an extension of the previous approximate analytical model^{7,8} to account for the effects of finite viscous penetration depth. Comparison to the numerical results shows that this new analytical model exhibits good accuracy for all viscous penetration depths for particles of high aspect ratio. We also compare these results to available experimental measurements and present a discussion pertinent to the interpretation of such measurements and future measurements.

2. PROBLEM DEFINITION AND FINITE-ELEMENT ANALYSIS

We consider an axisymmetric particle, immersed in a viscous fluid, that is undergoing symmetric extensional oscillations along its major axis, defined as the z -direction (see Figure 1). Three individual particle geometries, illustrated in Figure 1, are treated in detail. The first is a right circular cylinder, the simplest axisymmetric particle, which approximates the geometry of some gold nanorods that have been studied experimentally.^{7,12,24} The second is a conical cylinder, and the third is a truncated conical cylinder, or bipyramid, an approximation to the bipyramidal gold nanoparticles that have been studied experimentally.^{7,8}

Real metal nanoparticles have faceted surfaces and relatively complex cross-sections; for example, bipyramidal gold nanoparticles have pentagonal cross-sections.⁴⁶ The properties of extensional modes, however, are unlikely to be significantly affected by the details of the cross-section since the motion of the nanoparticle surface is primarily parallel to the long axis of the particles. We can therefore simplify the problem by

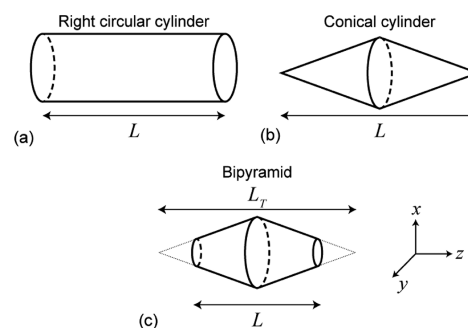


Figure 1. Schematic of the nanoparticle geometries that are modeled. (a) Right circular cylinder; (b) conical cylinder; (c) bipyramid (dotted lines are projections). All particles are axisymmetric with a maximum radius of R_{\max} and length L . The projected length of the bipyramid is L_T . The z -direction is along the length of the particle, and the origin is situated at the geometrical center of the particle.

approximating the particles as being axisymmetric, with circular cross-sections. For numerical simulations, symmetry in the particles allows the computational domain to be reduced to $z \geq 0$ only, where the origin is in the center of the particle. A schematic of this domain is given in Figure 2 for a bipyramid.

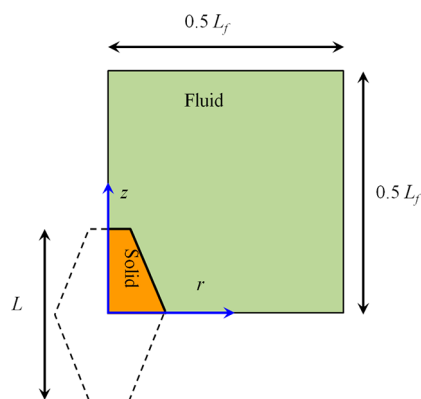


Figure 2. Schematic of a nanoparticle (bipyramid) immersed in a fluid, showing the computational domain and particle dimensions. The line along the z -direction through the major axis of the particle is the axis of symmetry. The fluid region is green, and the solid region is gold. The dashed region is not part of the computational domain and is shown only to illustrate the particle shape.

It is assumed that the oscillation amplitude of the particle is far smaller than any other geometric length scale, so that all nonlinear effects can be ignored.¹¹ This assumption is justified in practice⁴⁷ and dramatically simplifies the problem by (i) eliminating the need for Lagrangian tracking of the solid surface and (ii) enabling linearization of the equations of motion. The acoustic wavelength in the fluid is also assumed to greatly exceed the dominant hydrodynamic length scales, ensuring incompressible flow.⁷ The required governing equation for the fluid motion is thus the incompressible unsteady Stokes equation⁴⁸

$$\nabla \cdot \mathbf{v} = 0 \quad (1)$$

$$\rho \frac{\partial \mathbf{v}}{\partial t} = -\nabla p + \mu \nabla^2 \mathbf{v} \quad (2)$$

where \mathbf{v} is the fluid velocity field, p is the fluid pressure, ρ is the fluid density, μ is the fluid shear viscosity, t is time, and ∇ is the

spatial gradient operator. The corresponding equation for the solid is Navier's equation⁴⁹

$$\rho_s \frac{\partial^2 \mathbf{u}}{\partial t^2} = \frac{E}{2(1+\sigma)} \left\{ \nabla^2 \mathbf{u} + \frac{1}{(1-2\sigma)} \nabla(\nabla \cdot \mathbf{u}) \right\} \quad (3)$$

where \mathbf{u} is the solid displacement field, ρ_s is the solid density, E is Young's modulus, and σ is the Poisson ratio of the solid.

Since the motion is oscillatory, all time-dependent variables such as the solid displacement fluid velocity and fluid pressure can be expressed in terms of the explicit time dependence, $e^{-i\omega t}$

$$X(r, z, t) = \tilde{X}(r, z)\omega e^{-i\omega t} \quad (4)$$

where X denotes any of the time-dependent variables, ω is the radial frequency, t is time, and i is the usual imaginary unit. For simplicity, we henceforth omit the superfluous “ \sim ” notation, noting that the above relation holds universally.

At the interface between the fluid domain and the solid particle, the usual conditions of continuity of stress, velocity, and displacement are imposed, and the no-slip boundary condition is enforced. This provides direct coupling between the Navier–Stokes equation for the fluid, eq 2, and Navier's equation for the solid, eq 3. At boundaries far from the particle, the condition of zero fluid pressure is applied. This allows for flow into and out of these boundaries and thus presents a weaker condition than a no-penetration or no-slip condition, minimizing the effect of the finite computational domain.

The resulting coupled system of equations constitutes an eigenvalue problem in the complex frequency domain. The solution of this system is a complex eigenfrequency, ω , whose real and imaginary components, ω_r and ω_i , can be combined to give the resonant frequency, ω_f and quality factor, Q_f , of the corresponding vibrational mode

$$\omega_f = \sqrt{\omega_i^2 + \omega_r^2}, \quad Q_f = -\frac{\omega_f}{2\omega_i} \quad (5)$$

where the subscript f henceforth refers to the value in fluid; see the Supporting Information for a derivation of eq 5. We note that the intrinsic damping due to losses in the nanoparticle material itself is not considered here, but it can simply be added to the fluid damping, as expressed through the quality factor, Q_p , to obtain the total damping.⁷

The system of equations was implemented and solved in COMSOL using its damped eigenfrequency solver.⁵⁰ All results for ω_f and Q_f were converged to a tolerance of 99.9%. Computational domain dependence and mesh convergence studies are reported in the Supporting Information.

3. ANALYTICAL MODEL

We now provide an extension of the previously developed approximate analytical model^{7,8} to account for finite viscous penetration depth in the fluid surrounding the vibrating nanoparticle. Oscillation of the particle surface generates vorticity in the fluid that diffuses away from the surface, giving rise to a viscous penetration depth of finite extent. The previous model implicitly assumed that this penetration depth is infinitesimally small in comparison to the particle radius. This condition is now relaxed. All other assumptions of the original model are retained.

In particular, we still insist that the particle length greatly exceeds both the viscous penetration depth and particle radius, allowing for local approximation of the hydrodynamic load at any axial position along the particle. We thus divide the particle

into infinitesimal sections along its major axis and approximate each section by a circular cylinder. This enables the hydrodynamic load per unit length to be calculated: on each section the hydrodynamic load is given by that of a circular cylinder executing longitudinal oscillations along its major axis.⁴⁵ This analysis then gives the required hydrodynamic load per unit length in the z -direction

$$\begin{aligned} F_{\text{hydro}}(z) &= \int_{C_{\text{side}}} \mathbf{n}_s \cdot \boldsymbol{\sigma}_f \cdot \hat{\mathbf{z}} dl \\ &= \pi \mu \omega \frac{R(z)}{R_{\text{max}}} \sqrt{8i\beta(\omega)} \frac{K_1\left(-i\sqrt{2i\beta(\omega)} \frac{R(z)}{R_{\text{max}}}\right)}{K_0\left(-i\sqrt{2i\beta(\omega)} \frac{R(z)}{R_{\text{max}}}\right)} u(z) \end{aligned} \quad (6)$$

where $\boldsymbol{\sigma}_f$ is the stress tensor in the fluid, \mathbf{n}_s is an outward normal unit vector, $\hat{\mathbf{z}}$ is the unit vector in the z -direction, C_{side} is the circumference of the cross-section, dl is a circumferential line element, z is again the axial coordinate (see Figure 1), $R(z)$ is the position-dependent radius of the particle, R_{max} is the maximum particle radius, $u(z)$ is the position-dependent displacement of the particle in the z -direction, K_0 and K_1 are the modified Bessel functions of the third kind, and the dimensionless frequency β is defined as

$$\beta(\omega) = \frac{\rho \omega R_{\text{max}}^2}{2\mu} \quad (7)$$

With the hydrodynamic load determined, the calculation proceeds in an identical manner to that previously presented,^{7,8} yielding the required expression for the normalized complex eigenfrequency

$$\begin{aligned} \bar{\omega}^2 &\equiv \left(\frac{L^2 \rho_s}{E} \right) \omega^2 \\ &= \frac{\int_0^{1/2} R^2(z) (u'(z))^2 dz}{\int_0^{1/2} \left(R^2(z) + (1+i) \frac{\rho}{\rho_s} R_{\text{max}} R(z) \sqrt{\frac{1}{\beta(\omega)}} K^*(\omega, z) \right) u^2(z) dz} \end{aligned} \quad (8)$$

where $K^*(\omega, z) = K_1(-i(2i\beta(\omega))^{1/2} R(z)/R_{\text{max}})/K_0(-i(2i\beta(\omega))^{1/2} R(z)/R_{\text{max}})$. We assume that stress in the solid greatly exceeds that in the fluid (see below), so that the displacement $u(z)$ is the result in the absence of fluid. This coincides with the mode shape in vacuum.

For a right circular cylinder, the particle radius is constant: $R(z) = R_{\text{max}}$. This allows for analytical evaluation of the integrals in eq 8. For the fundamental extensional mode this gives

$$\bar{\omega}^2 \equiv \left(\frac{L^2 \rho_s}{E} \right) \omega^2 = \frac{\bar{\omega}_{\text{vac}}^2}{1 + \frac{\rho}{\rho_s} \Gamma(\omega)} \quad (9)$$

with

$$\Gamma_r(\omega) = \frac{K_r^*(\omega) - K_i^*(\omega)}{\sqrt{\beta(\omega)}}, \quad \Gamma_i(\omega) = \frac{K_r^*(\omega) + K_i^*(\omega)}{\sqrt{\beta(\omega)}} \quad (10)$$

where $\bar{\omega}_{\text{vac}} = \pi$ is the normalized radial resonant frequency of the particle in vacuum, and the function K^* is as defined above, but is now independent of z . The subscripts r and i again refer to the real and imaginary components. Equations 9 and 10

constitute a transcendental equation for the complex eigenfrequency, ω . In the limit of high β , the results in eq 10 reduce to those derived previously.⁸

For conical cylinders or bipyramids, the integrals in eq 8 must be evaluated numerically. In the Supporting Information, we provide empirical fits to the numerically computed functions, which can be used for rapid evaluation of the frequency and damping factor.

4. DIMENSIONAL ANALYSIS

Through dimensional analysis, we can derive scaling relations that allow us to normalize calculated results for the resonant frequency and quality factor. This is simplified by the assumption that the mechanical stress in the solid particle greatly exceeds that in the fluid, so that the fluid does not significantly affect the vibrational mode shapes of the particles. Comparing expressions for the stress in the solid and the fluid, this assumption translates into the requirement that $\mu\omega/E \ll 1$. This assumption is valid in many cases of practical interest, including in particular the important case of metal nanoparticles in low-viscosity fluids.^{6–8,12,19,28} An extended treatment would be required for the vibrations of soft nanoparticles or fluids of high viscosity, as we discuss below.

Since we assume that the mode shape is unaffected by the fluid, it follows that the net strain energy within the particle is also independent of the fluid properties.⁵¹ Vibration of the particle accelerates the fluid, which increases the effective mass of the vibrating particle. Equating the strain energies of the particle in the presence and absence of fluid then gives

$$m_{\text{eff}}\omega_{\text{vac}}^2 = (m_{\text{eff}} + m_{\text{added}})\omega_f^2 \quad (11)$$

where m_{eff} is the effective mass of the particle in vacuum, m_{added} is the additional effective mass due to acceleration of the fluid, ω_{vac} is the resonant frequency in vacuum, and ω_f is the resonant frequency in fluid. We define $m_{\text{eff}} = \rho_s V_s$ and $m_{\text{added}} = \rho V_f$, where V_s and V_f are the effective volumes of the solid and fluid, respectively. The particle effective mass, m_{eff} , is linearly proportional to the particle density, ρ_s , whereas m_{added} has a more complicated dependence on fluid density ρ and viscosity μ .¹¹ The normalized inertial component of the hydrodynamic load can then be determined from eq 11

$$\Lambda(\omega_f) \equiv \frac{V_f}{V_s} = \frac{\rho_s}{\rho} \left\{ \left(\frac{\omega_{\text{vac}}}{\omega_f} \right)^2 - 1 \right\} \quad (12)$$

From dimensional considerations, $\Lambda(\omega_f)$ must depend on the particle aspect ratio, L/R_{max} , the normalized frequency, $\beta_f \equiv \beta(\omega_f) = \rho\omega_f R_{\text{max}}^2/(2\mu)$, and Poisson's ratio, σ . Since we assume $\mu\omega/E \ll 1$, the dimensionless parameter $\mu\omega/E$ does not affect $\Lambda(\omega)$. Formally, β is the square of the ratio of the particle radius to the viscous penetration depth over which vorticity diffuses from the particle surface.

The quality factor, Q_f , gives a scaled measure of the energy dissipation, relating the maximum energy stored in the particle to the energy dissipated per cycle. Through use of dimensional analysis and the Buckingham π theorem,⁵² a rigorous expression for the energy dissipated per cycle can be derived:^{53,54} $E_{\text{diss}} = \rho V_f \Phi(\omega) Q_f \omega^2 A^2$, where A is the oscillation amplitude, ω is the radial oscillation frequency, and $\Phi(\omega)$ is a dimensionless function that depends on β .^{11,53} Formally, $\Phi(\omega)$ is the nondimensionalized rate of energy dissipation in the fluid; dimensional analysis shows that this depends on a second

dimensionless group, β , defined above. For details of this derivation, the reader is referred to refs 53 and 54.

Substituting this result for E_{diss} into the definition for the quality factor, $Q_f = 2\pi(E_{\text{stored}}/E_{\text{diss}})|_{\omega=\omega_f}$, where E_{stored} is the maximum energy stored in the vibrating particle, gives the normalized dissipative component

$$\Omega(\omega_f) \equiv \Phi(\omega_f) \frac{V_f}{V_s} = \frac{\rho_s}{\rho} \left(\frac{\omega_{\text{vac}}}{\omega_f} \right)^2 \frac{1}{Q_f} \quad (13)$$

Note that $\Omega(\omega_f)$ and $\Lambda(\omega_f)$ also depend on the particle aspect ratio, normalized frequency, and Poisson's ratio.

The resonant frequency and quality factor for a particle of general composition and size that is immersed in a viscous fluid can be determined by evaluating the dimensionless functions $\Lambda(\omega)$ and $\Omega(\omega)$ and using eqs 12 and 13. For the special case of a right circular cylinder with large aspect ratio, eqs 9, 12, and 13 give $\Gamma_r(\omega) = \Lambda(\omega)$ and $\Gamma_i(\omega) = \Omega(\omega)$. This illustrates the utility of the scaling analysis.

5. RESULTS

We now present numerical data for the resonant frequency and quality factor of a particle immersed in fluid using the finite-element analysis described above. Results are given for the dimensionless functions in eqs 12 and 13, enabling calculation of the resonant frequency and quality factor for general fluid properties, particle composition, and size. The fundamental extensional mode is considered throughout. These results are compared to the approximate analytical models that assume (i) thin viscous penetration depth^{7,8} and (ii) finite viscous penetration depth (above). Results are presented for right circular cylinders, conical cylinders, and bipyramids with $L/L_T = 0.75$. Particles with aspect ratios, L/R_{max} , ranging from 4.8 to 200 are considered, covering the typical range of geometries encountered in practice.^{7,12,24} We consider density ratios, ρ_s/ρ , from 1 to 1000 and Poisson's ratios, σ , from 0 to 0.49. As mentioned above, we require the mechanical stress in the particle to greatly exceed that in the fluid; simulations were thus restricted to the regime $\mu\omega/E < 0.001$. Results are presented for $Q_f \geq 1$.

5.1. Right Circular Cylinders with Large Aspect Ratios.

To begin, we illustrate the effects of varying the fluid and solid properties on the resonant frequency and quality factor of a right circular cylinder with large aspect ratio, $L/R_{\text{max}} = 200$. The results, shown in Figure 3, illustrate the interplay between the density ratio of the solid particle and surrounding fluid, ρ_s/ρ , and the normalized frequency, $\beta_f \equiv \rho\omega_f R_{\text{max}}^2/(2\mu)$; we remind the reader that β_f refers to the value of $\beta(\omega)$ evaluated at the resonant frequency in fluid, ω_f .

The normalized frequency, β_f , is the squared ratio of the particle radius to the viscous penetration depth. Increasing β_f for a fixed ρ_s/ρ thus reduces the effect of viscosity and leads to an increase in both the resonant frequency and quality factor (see Figure 3). In the limit $\beta_f \rightarrow \infty$, energy dissipation is eliminated, and the effects of viscosity are removed. Nonetheless, the inertial component of the fluid load remains finite in this limit, leading to reduction in the resonant frequency relative to the frequency in vacuum, ω_{vac} (see Figure 3a). Results in this inviscid limit are explored further in the Supporting Information (Figure S2).

The density ratio, ρ_s/ρ , governs the relative strength of inertia in the fluid to inertia in the solid. As ρ_s/ρ is increased for a fixed β_f , the effects of the fluid again decrease. However, as

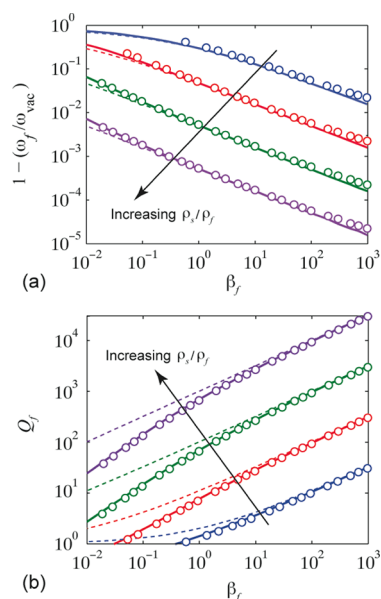


Figure 3. Calculated values for (a) the normalized resonant frequency and (b) quality factor for extensional vibrations of a right circular cylinder with aspect ratio $L/R_{\max} = 200$, immersed in a viscous fluid, as a function of normalized frequency, β_f . Data are given for solid-to-fluid density ratios of $\rho_s/\rho = 1$ (blue), 10 (red), 100 (green), and 1000 (purple). Results are shown for Poisson's ratio $\sigma = 0$ but were found to be insensitive to σ . Open circles are finite-element results; dashed lines are calculated using an analytical model that assumes a thin viscous penetration depth; solid lines are calculated using an analytical model that takes into account the finite viscous penetration depth (eqs 9, 12, and 13).

$\rho_s/\rho \rightarrow \infty$, the resonant frequency approaches ω_{vac} because fluid inertia no longer contributes to the total inertia. The quality factor also increases as ρ_s/ρ increases because fluid effects are diminished relative to the energy stored in the particle (see Figure 3b).

The results in Figure 3b clearly demonstrate that the model assuming thin viscous penetration depths works well in the limit $\beta_f \gg 1$, as expected, but exhibits significant discrepancy as β_f is reduced. The new model incorporating the effects of finite viscous penetration depth dramatically improves on this result and yields excellent agreement over the entire range of β_f studied.

Even so, both analytical models erroneously predict that the resonant frequency approaches ω_{vac} as $\beta_f \rightarrow \infty$. Importantly, the models are derived for a slender particle ($L/R_{\max} \gg 1$) and ignore the pressure load at the particle ends. This pressure load reduces the resonant frequency by enhancing the inertial component of the hydrodynamic load, which does not vanish in the inviscid limit $\beta_f \rightarrow \infty$. Rigorous analytical calculation of this load presents a significant challenge, but its effects can be quantitatively characterized by comparison to finite-element calculations. The net pressure load in this limit, $\beta_f \rightarrow \infty$, is found to scale with the inverse aspect ratio, R_{\max}/L ; see the Supporting Information for details.

The Poisson's ratio of the solid is found to have a negligible effect on the resonant frequency and quality factor of a slender particle, i.e., for $L/R_{\max} \gg 1$. Nonzero Poisson's ratio results in lateral contraction of the particle in response to a longitudinal extension. From dimensional considerations, the effect of this additional motion on the net hydrodynamic load is expected to be of $O(R_{\max}/L) \ll 1$.

5.2. Particles with Smaller Aspect Ratios. Next, we present results for the dimensionless functions, $\Lambda(\omega)$ and $\Omega(\omega)$, for right circular cylinders, conical cylinders, and bipyramids with $L/L_T = 0.75$. These dimensionless functions were calculated from results for the resonant frequency and quality factor, using the definitions in eqs 12 and 13. For simplicity, the density ratio was set to $\rho_s/\rho = 20$, which is typical for the practical case of gold nanoparticles immersed in liquid;^{6–8,12,19,28} varying this value between 1 and 100 did not affect the resulting dimensionless functions, as expected.

In Figure 4, results are given as a function of the normalized frequency, β_f , for right circular cylinders with different aspect

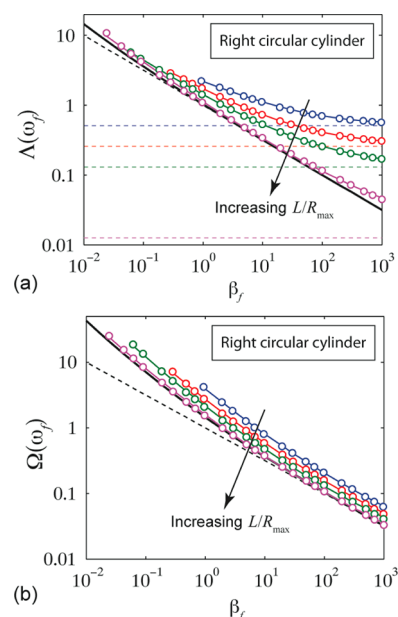


Figure 4. Calculated values for (a) the inertial component, $\Lambda(\omega)$, and (b) the dissipative component, $\Omega(\omega)$, of the hydrodynamic load on a right circular cylinder, as a function of normalized frequency, β_f . Results are shown for particle aspect ratios $L/R_{\max} = 5$ (blue), 10 (red), 20 (green), and 200 (purple), and for Poisson's ratio $\sigma = 0$. Open circles are finite-element results (solid lines connecting open circles of the same color are fits to guide the eye); dashed (nonhorizontal) black lines are calculated using an analytical model that assumes a thin viscous penetration depth; solid black lines are calculated using an analytical model that takes into account the finite viscous penetration depth (eqs 9, 12, and 13); horizontal dashed lines in (a) of the same color as the open circles are results for an inviscid fluid ($\beta_f \rightarrow \infty$, see the Supporting Information for details).

ratios, L/R_{\max} . As the aspect ratio decreases, both the inertial and dissipative functions, $\Lambda(\omega)$ and $\Omega(\omega)$, increase. This effect is more pronounced for $\Lambda(\omega)$ at high inertia ($\beta_f \gg 1$), where (inviscid) pressure effects at the particle ends manifest themselves most strongly. In other words, incorporation of end effects is vital for calculation of the resonant frequency for particles with relatively small aspect ratios, in the presence of thin viscous boundary layers. Such inviscid effects are not significant for the dissipative component, $\Omega(\omega)$ (see Figure 4b).

Analogous results for conical cylinders and bipyramids are given in Figure 5. While the inertial function, $\Lambda(\omega)$, exhibits trends similar to those found for the circular cylinder in Figure 4a, the dissipative function, $\Omega(\omega)$, is insensitive to particle aspect ratio (see Figure 5b). The new approximate model for

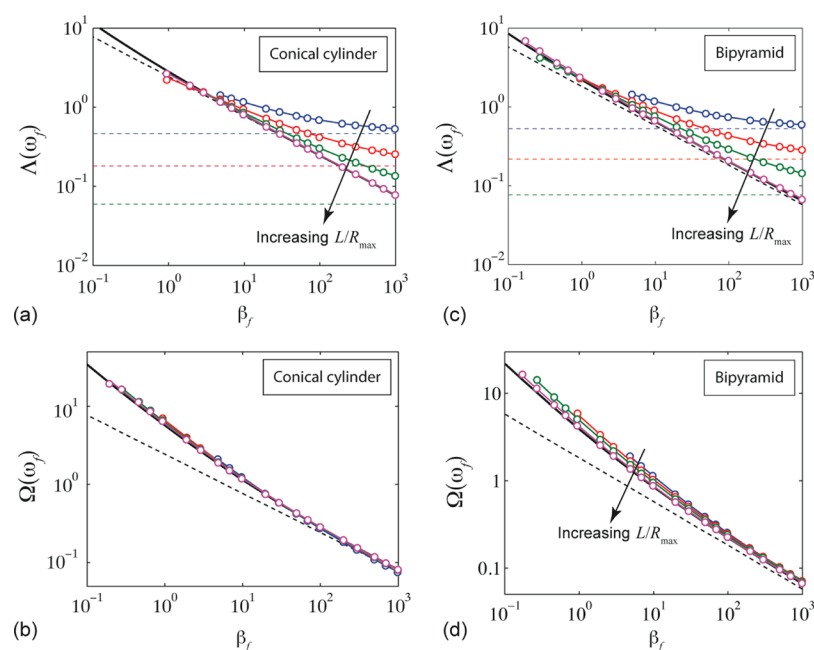


Figure 5. Same as for Figure 4, but results are now given for (a, b) conical cylinders and (c, d) bipyramids with $L/L_T = 0.75$. Also, results for the model with finite viscous penetration depth are now calculated using eq 8; data are given in the Supporting Information.

Table 1. Comparison of Calculated Quality Factors to Experimental Values Reported in the Literature^a

reference	liquid	Q_{meas}	$Q_{\text{f}}^{\text{orig}}$	Q_{f}^{FE}	Q_{int}
Pelton	water	15.7 ± 0.6	40.9 ± 3	23.7 ± 1.2	46.5 ± 1
Pelton	methanol	17.3 ± 2.4	58.6 ± 2.2	35.2 ± 0.8	34.0 ± 9
Pelton	ethylene glycol	8.6 ± 0.8	9.9 ± 0.5	2.9 ± 0.1	-
Pelton	glycerine	1.6 ± 0.6	2.1 ± 0.1	0.5	-
Ruijgrok	water	19 ± 1.7	48.6 ± 0.4	18.4 ± 0.2	-

^aPelton: ref 7; Ruijgrok: ref 12. Q_{meas} is the experimentally measured quality factor; $Q_{\text{f}}^{\text{orig}}$ is the quality factor due to fluid damping according to the original analytical model,^{7,8} which assumes a thin viscous penetration depth; Q_{f}^{FE} is the quality factor due to fluid damping predicted by finite-element calculations; and Q_{int} is the intrinsic quality factor inferred from Q_{meas} and Q_{f}^{FE} . No result is given for Q_{int} when $Q_{\text{meas}} \geq Q_{\text{f}}^{\text{FE}}$.

finite viscous penetration depth accurately predicts the finite-element results for all the aspect ratios considered. Particularly good agreement is found for conical cylinders. These particles have zero pressure loads at their ends, due to their geometry, and we find that $\Omega(\omega)$ is nearly independent of aspect ratio. This contrasts strongly to the results for a right circular cylinder, discussed above. Results for the bipyramidal cylinder are intermediate between these two cases: the ends of these particles have a small but finite area, and $\Omega(\omega)$ depends weakly on aspect ratio (see Figure 5d).

The results given in Figures 4 and 5 are for a Poisson's ratio of zero. Poisson's ratio was found to exert a small effect in all cases studied, which encompass the typical practical range of particle aspect ratios. Nonetheless, its influence does increase for smaller aspect ratios, i.e., for $L/R_{\text{max}} \leq 5$, because the effects of lateral deformations become more significant; additional results are shown in the Supporting Information.

6. COMPARISON TO MEASUREMENTS

The finite-element results presented in this article are now used to interpret recent experimental measurements of the fundamental extensional mode of nanoparticles in fluid.

Quality factors were measured previously for the extensional vibrations of bipyramidal gold nanoparticles and were interpreted using the original model that implicitly assumes thin viscous penetration depths.⁷ Table 1 shows the measured

(total) quality factors, Q_{tot} , and the quality factors due to the fluid only, $Q_{\text{f}}^{\text{orig}}$, calculated according to this original model, for different fluids. The measured and modeled results were compared using a single fit parameter, Q_{int} , that describes dissipation intrinsic to the nanoparticles themselves. That is, the total damping was simply taken to be a sum of this intrinsic damping and the fluid damping

$$\frac{1}{Q_{\text{tot}}} = \frac{1}{Q_{\text{int}}} + \frac{1}{Q_{\text{f}}} \quad (14)$$

Good agreement was previously obtained for all measurements using $Q_{\text{int}} = 25 \pm 3$.⁷ These findings are now reassessed using the finite-element results of the present study. Results for the new analytical model are not given since it is less accurate than the finite-element results and its error is quantified above. Measurements that were performed in a follow-up article⁸ agree with these original measurements and are therefore not analyzed here.

Fluid quality factors, Q_{f}^{FE} , determined using the finite-element calculations are given in Table 1. A Poisson's ratio of 0.44 was used in all simulations; varying this value had a weak effect, as discussed above. For bipyramids in water, the finite-element analysis gives $Q_{\text{f}} = 23.7 \pm 1.2$. This is significantly lower than the prediction of the original model ($Q_{\text{f}} = 40.9 \pm 3$), reflecting enhanced energy dissipation due to the finite viscous

penetration depth. Combining the finite-element result with the measured quality factor gives a new estimate for the intrinsic quality factor: $Q_{\text{int}} = 46.5 \pm 1$. Performing a similar analysis for methanol yields a revised value of $Q_{\text{int}} = 34 \pm 9$, which is consistent with the result for water within the measurement uncertainty.

In contrast to water and methanol, which have comparable viscosities, ethylene glycol has a viscosity an order of magnitude larger. The fluid stress parameter for ethylene glycol is still small, $\mu\omega/E = 0.025 \ll 1$, but larger than the upper bound considered in the simulations presented above. Further finite-element simulations were therefore necessary to model this case and gave $Q_f = 2.9 \pm 0.1$. This new prediction is less than the measured quality factor, which means that finite-element results cannot explain the measurement results. Glycerine has a viscosity 2 orders of magnitude higher still, corresponding to a stress value of $\mu\omega/E = 1.4$. Significant modification of the mode shape is therefore expected, which will in turn affect the quality factor. Time domain finite-element simulations (see the Supporting Information) that account for this value of $\mu\omega/E$ give a prediction of $Q_f = 0.5$, corresponding to a strongly overdamped system. This value is significantly smaller than the measured quality factor, which displayed an under-damped response. We note that care must also be taken to interpret measurements at low quality factor since frequency dependence of the hydrodynamic load can exert a strong effect.¹¹ Nonetheless, the anomalous results for high-viscosity fluids suggest the presence of nonstandard effects that can decrease energy dissipation in the fluid, such as slip at the solid–liquid boundary. Analysis of such effects presents an interesting area for future investigation.

Finally, we analyze the results of Ruijgrok et al.,¹² who presented a single measurement of the quality factor for the extensional mode of a rod-shaped nanoparticle with aspect ratio $L/R_{\text{max}} = 5$ immersed in water. Approximating the nanorod as a right circular cylinder gives a fluid quality factor that coincides with the measured quality factor, as shown in Table 1. This suggests that damping due to the surrounding water greatly exceeds the intrinsic damping within the particle, in contrast to the results discussed above for bipyramidal nanoparticles. Any slip at the solid–liquid interface would increase the fluid quality factor; this would mean that more intrinsic damping would be required to explain the experimental results, making them more consistent with the results for bipyramids. We emphasize, however, that this interpretation is based on a single reported measurement, and additional measurements are clearly needed before firm conclusions can be drawn.

7. CONCLUSIONS

We have presented a theoretical investigation of the extensional acoustic vibrations of axisymmetric nanoparticles immersed in viscous fluids. This included rigorous finite-element results for right circular cylinders, conical cylinders, and bipyramids. A new, approximate analytical model was also developed, which builds on a previous model for particles with large aspect ratio,⁷ but which now accounts for finite viscous penetration depth in the fluid surrounding the particle. The results validate the original analytical model for particles of large aspect ratio when the viscous penetration depth is small relative to the particle radius. The new analytical model significantly improves on this original model, providing a more accurate means of predicting the quality factors of nanoparticles for a wider range of aspect ratios and fluid viscosities. The finite-element results provide

the most accurate solution and are thus the most appropriate to apply in practice when assessing experimental results. This application is facilitated by the use of the dimensionless numerical results that we have provided.

We compared these finite-element results to available experimental results in the literature. Comparison to published measurements on bipyramidal gold nanoparticles showed that the finite-element calculations can account for the measured damping in low viscosity liquids, such as water and methanol. Significant discrepancies were observed for bipyramids in higher viscosity liquids, and results for a rod-shaped nanoparticle immersed in water were inconsistent with the corresponding bipyramid measurements. Further measurements on particles of different shape immersed in fluids of different viscosity are required to gain insight into the origins of these discrepancies, particularly at high viscosities, where slip at the solid–liquid interface may be significant. The results presented in this study provide a foundation for the interpretation of such future measurements, which will provide a rigorous understanding of the effects of particle shape and composition on energy dissipation within the nanoparticles and due to the surrounding fluid.

■ ASSOCIATED CONTENT

Supporting Information

Derivation of eq 5; tests of domain independence and mesh convergence for the finite-element calculations; validation of the numerical method; empirical functions for $\Gamma(\omega)$ of conical and bipyramidal cylinders; model results in the inviscid limit; numerical and analytical results similar to Figure 3 for conical and bipyramidal nanoparticles; fit function to finite-element results; time-domain simulation for very high viscosity. This material is available free of charge via the Internet at <http://pubs.acs.org>.

■ AUTHOR INFORMATION

Corresponding Author

*E-mail: jsader@unimelb.edu.au.

Notes

The authors declare no competing financial interest.

■ ACKNOWLEDGMENTS

This research was supported by the Australian Research Council Grants Scheme. This work was performed, in part, at the Center for Nanoscale Materials, a U.S. Department of Energy, Office of Science, Office of Basic Energy Sciences User Facility under Contract No. DE-AC02-06CH11357.

■ REFERENCES

- (1) Still, T.; Sainidou, R.; Retsch, M.; Jonas, U.; Spahn, P.; Hellmann, G. P.; Fytas, G. The “Music” of Core–Shell Spheres and Hollow Capsules: Influence of the Architecture on the Mechanical Properties at the Nanoscale. *Nano Lett.* **2008**, *8*, 3194–3199.
- (2) Portales, H. Probing Atomic Ordering and Multiple Twinning in Metal Nanocrystals through Their Vibrations. *Proc. Natl Acad. Sci. U.S.A.* **2008**, *105*, 14784–14789.
- (3) Fujii, M.; Nagareda, T.; Hayashi, S.; Yamamoto, K. Low-Frequency Raman Scattering from Small Silver Particles Embedded in SiO₂ Thin Films. *Phys. Rev. B* **1991**, *44*, 6243–6248.
- (4) Palpant, B.; Portales, H.; Saviot, L.; Lermé, J.; Prével, B.; Pellarin, M.; Duval, E.; Perez, A.; Broyer, M. Quadrupolar Vibrational Mode of Silver Clusters from Plasmon-Assisted Raman Scattering. *Phys. Rev. B* **1999**, *60*, 17107–17111.

- (5) Pelton, M.; Aizpurua, J.; Bryant, G. W. Metal-Nanoparticle Plasmonics. *Laser Photonics Rev.* **2008**, *2*, 135–169.
- (6) Pelton, M.; Liu, M. Z.; Kim, H. Y.; Smith, G.; Guyot-Sionnest, P.; Scherer, N. E. Optical Trapping and Alignment of Single Gold Nanorods by Using Plasmon Resonances. *Opt. Lett.* **2006**, *31*, 2075–2077.
- (7) Pelton, M.; Sader, J. E.; Burgin, J.; Liu, M. Z.; Guyot-Sionnest, P.; Gosztola, D. Damping of Acoustic Vibrations in Gold Nanoparticles. *Nat. Nanotechnol.* **2009**, *4*, 492–495.
- (8) Pelton, M.; Wang, Y.; Gosztola, D.; Sader, J. E. Mechanical Damping of Longitudinal Acoustic Oscillations of Metal Nanoparticles in Solution. *J. Phys. Chem. C* **2011**, *115*, 23732–23740.
- (9) Green, C. P.; Sader, J. E. Torsional Frequency Response of Cantilever Beams Immersed in Viscous Fluids with Applications to the Atomic Force Microscope. *J. Appl. Phys.* **2002**, *92*, 6262–6274.
- (10) Sader, J.; Burg, T.; Manalis, S. Energy Dissipation in Microfluidic Beam Resonators. *J. Fluid Mech.* **2010**, *650*, 215.
- (11) Sader, J. E. Frequency Response of Cantilever Beams Immersed in Viscous Fluids with Applications to the Atomic Force Microscope. *J. Appl. Phys.* **1998**, *84*, 64–76.
- (12) Ruijgrok, P. V.; Zijlstra, P.; Tchegbotareva, A. L.; Orrit, M. Damping of Acoustic Vibrations of Single Gold Nanoparticles Optically Trapped in Water. *Nano Lett.* **2012**, *12*, 1063–1069.
- (13) Nisoli, M.; De Silvestri, S.; Cavalleri, A.; Malvezzi, A. M.; Stella, A.; Lanzani, G.; Cheysson, P.; Kofman, R. Coherent Acoustic Oscillations in Metallic Nanoparticles Generated with Femtosecond Optical Pulses. *Phys. Rev. B* **1997**, *55*, R13424–R13427.
- (14) Del Fatti, N.; Voisin, C.; Chevy, F.; Vallée, F.; Flytzanis, C. Coherent Acoustic Mode Oscillation and Damping in Silver Nanoparticles. *J. Chem. Phys.* **1999**, *110*, 11484–11487.
- (15) Hodak, J. H.; Henglein, A.; Hartland, G. V. Photophysics of Nanometer Sized Metal Particles: Electron-Phonon Coupling and Coherent Excitation of Breathing Vibrational Modes. *J. Phys. Chem. B* **2000**, *104*, 9954–9965.
- (16) Del Fatti, N.; Voisin, C.; Christofilos, D.; Vallée, F.; Flytzanis, C. Acoustic Vibration of Metal Films and Nanoparticles. *J. Phys. Chem. A* **2000**, *104*, 4321–4326.
- (17) Hartland, G. V. Measurements of the Material Properties of Metal Nanoparticles by Time-resolved Spectroscopy. *Phys. Chem. Chem. Phys.* **2004**, *6*, 5263–5274.
- (18) Hartland, G. V. Coherent Excitation of Vibrational Modes in Metallic Nanoparticles. *Annu. Rev. Phys. Chem.* **2006**, *57*, 403–430.
- (19) Hartland, G. V. Optical Studies of Dynamics in Noble Metal Nanostructures. *Chem. Rev.* **2011**, *111*, 3858–3887.
- (20) Juvé, V.; Crut, A. L.; Maioli, P.; Pellarin, M.; Broyer, M.; Del Fatti, N.; Vallée, F. Probing Elasticity at the Nanoscale: Terahertz Acoustic Vibration of Small Metal Nanoparticles. *Nano Lett.* **2010**, *10*, 1853–1858.
- (21) Zijlstra, P.; Tchegbotareva, A.; Chon, J.; Gu, M.; Orrit, M. Acoustic Oscillations and Elastic Moduli of Single Gold Nanorods. *Nano Lett.* **2008**, *8*, 3493–3497.
- (22) Hodak, J. H.; Henglein, A.; Hartland, G. V. Size Dependent Properties of Au Particles: Coherent Excitation and Dephasing of Acoustic Vibrational Modes. *J. Chem. Phys.* **1999**, *111*, 8613–8621.
- (23) Voisin, C.; Del Fatti, N.; Christofilos, D.; Vallée, F. Time-Resolved Investigation of the Vibrational Dynamics of Metal Nanoparticles. *Appl. Surf. Sci.* **2000**, *164*, 131–139.
- (24) Hu, M.; Wang, X.; Hartland, G. V.; Mulvaney, P.; Juste, J. P.; Sader, J. E. Vibrational Response of Nanorods to Ultrafast Laser Induced Heating: Theoretical and Experimental Analysis. *J. Am. Chem. Soc.* **2003**, *125*, 14925–14933.
- (25) Ekinici, K. L.; Roukes, M. L. Nanoelectromechanical Systems. *Rev. Sci. Instrum.* **2005**, *76*, 061101.
- (26) Craighead, H. G. Nanoelectromechanical Systems. *Science* **2000**, *290*, 1532–1535.
- (27) Bunch, J. S.; van der Zande, A. M.; Verbridge, S. S.; Frank, I. W.; Tanenbaum, D. M.; Parpia, J. M.; Craighead, H. G.; McEuen, P. L. Electromechanical Resonators from Graphene Sheets. *Science* **2007**, *315*, 490–493.
- (28) Burg, T. P.; Godin, M.; Knudsen, S. M.; Shen, W.; Carlson, G.; Foster, J. S.; Babcock, K.; Manalis, S. R. Weighing of Biomolecules, Single Cells and Single Nanoparticles in Fluid. *Nature* **2007**, *446*, 1066–1069.
- (29) Chiu, H.-Y.; Hung, P.; Postma, H. W. C.; Bockrath, M. Atomic-Scale Mass Sensing Using Carbon Nanotube Resonators. *Nano Lett.* **2008**, *8*, 4342–4346.
- (30) Lavrik, N. V.; Sepaniak, M. J.; Datskos, P. G. Cantilever Transducers as a Platform for Chemical and Biological Sensors. *Rev. Sci. Instrum.* **2004**, *75*, 2229–2253.
- (31) Juan, M. L.; Righini, M.; Quidant, R. Plasmon Nano-Optical Tweezers. *Nat. Photonics* **2011**, *5*, 349–356.
- (32) Jensen, K.; Kim, K.; Zettl, A. An Atomic-Resolution Nano-mechanical Mass Sensor. *Nat. Nanotechnol.* **2008**, *3*, 533–537.
- (33) Peng, H. B.; Chang, C. W.; Aloni, S.; Yuzvinsky, T. D.; Zettl, A. Ultrahigh Frequency Nanotube Resonators. *Phys. Rev. Lett.* **2006**, *97*, 087203.
- (34) Naik, A. K.; Hanay, M. S.; Hiebert, W. K.; Feng, X. L.; Roukes, M. L. Towards Single-Molecule Nanomechanical Mass Spectrometry. *Nat. Nanotechnol.* **2009**, *4*, 445–450.
- (35) Yang, Y. T.; Callegari, C.; Feng, X. L.; Ekinici, K. L.; Roukes, M. L. Zeptogram-Scale Nanomechanical Mass Sensing. *Nano Lett.* **2006**, *6*, 583–586.
- (36) Arlett, J. L.; Roukes, M. L. Ultimate and Practical Limits of Fluid-Based Mass Detection with Suspended Microchannel Resonators. *J. Appl. Phys.* **2010**, *108*, 084701.
- (37) Arlett, J. L.; Myers, E. B.; Roukes, M. L. Comparative Advantages of Mechanical Biosensors. *Nat. Nanotechnol.* **2011**, *6*, 203–215.
- (38) Eichler, A.; Moser, J.; Chaste, J.; Zdrojek, M.; Wilson Rae, I.; Bachtold, A. Nonlinear Damping in Mechanical Resonators Made from Carbon Nanotubes and Graphene. *Nat. Nanotechnol.* **2011**, *6*, 339–342.
- (39) Van Eysden, C. A.; Sader, J. E. Frequency Response of Cantilever Beams Immersed in Compressible Fluids with Applications to the Atomic Force Microscope. *J. Appl. Phys.* **2009**, *106*, 094904.
- (40) van Dijk, M. A.; Lippitz, M.; Orrit, M. Detection of Acoustic Oscillations of Single Gold Nanospheres by Time-Resolved Interferometry. *Phys. Rev. Lett.* **2005**, *95*, 267406.
- (41) Staleva, H.; Hartland, G. V. Transient Absorption Studies of Single Silver Nanocubes. *J. Phys. Chem. C* **2008**, *112*, 7535–7539.
- (42) Staleva, H.; Hartland, G. V. Vibrational Dynamics of Silver Nanocubes and Nanowires Studied by Single-Particle Transient Absorption Spectroscopy. *Adv. Funct. Mater.* **2008**, *18*, 3809–3817.
- (43) Guillet, Y.; Rossignol, C.; Audoin, B.; Calbris, G.; Ravaine, S. Optoacoustic Response of a Single Submicronic Gold Particle Revealed by the Picosecond Ultrasonics Technique. *Appl. Phys. Lett.* **2009**, *95*, 061909–3.
- (44) Marty, R.; Arbouet, A.; Girard, C.; Mlayah, A.; Paillard, V.; Lin, V. K.; Teo, S. L.; Tripathy, S. Damping of the Acoustic Vibrations of Individual Gold Nanoparticles. *Nano Lett.* **2011**, *11*, 3301–3306.
- (45) Stokes, G. G. On the Effect of the Internal Friction of Fluids on the Motion of Pendulums. *Trans. Cambridge Philos. Soc.* **1851**, *9*, 8.
- (46) Liu, M. Z.; Guyot-Sionnest, P. Mechanism of Silver(I)-Assisted Growth of Gold Nanorods and Bipyramids. *J. Phys. Chem. B* **2005**, *109*, 22192–22200.
- (47) Hartland, G. V. Coherent Vibrational Motion in Metal Particles: Determination of the Vibrational Amplitude and Excitation Mechanism. *J. Chem. Phys.* **2002**, *116*, 8048–8055.
- (48) Batchelor, G. K. *An Introduction to Fluid Dynamics*, 1st ed.; Cambridge University Press: Cambridge, UK, 1967.
- (49) Landau, L. D.; Lifshitz, E. M. *Theory of Elasticity*, 3rd ed.; Butterworth-Heinemann: Boston, MA, USA, 1986.
- (50) COMSOL Multiphysics, Gottingen, Germany.
- (51) Timoshenko, S. P.; Goodier, J. N. *Theory of Elasticity*, 3rd ed.; McGraw-Hill: New York, 1969.
- (52) Buckingham, E. On Physically Similar Systems; Illustrations of the Use of Dimensional Equations. *Phys. Rev.* **1914**, *4*, 345–376.

(53) Sader, J. E.; Sanelli, J. A.; Adamson, B. D.; Monty, J. P.; Wei, X.; Crawford, S. A.; Friend, J. R.; Marusic, I.; Mulvaney, P.; Bieske, E. J. Spring Constant Calibration of Atomic Force Microscope Cantilevers of Arbitrary Shape. *Rev. Sci. Instrum.* **2012**, *83*, 103705.

(54) Sader, J. E.; Pacifico, J.; Green, C. P.; Mulvaney, P. General Scaling Law for Stiffness Measurement of Small Bodies with Applications to the Atomic Force Microscope. *J. Appl. Phys.* **2005**, *97*, 124903.